J. Fluid Mech. (1998), *vol.* 355, *pp.* 17–44. Printed in the United Kingdom

© 1998 Cambridge University Press

An experimental investigation of meniscus roll coating

By P. H. GASKELL[1], G. E. INNES[1] AND M. D. SAVAGE[2]

[1]Department of Mechanical Engineering, University of Leeds, Leeds LS2 9JT, UK

[2]Department of Physics and Astronomy, University of Leeds, Leeds LS2 9JT, UK

(Received 28 March 1996 and in revised form 13 February 1997)

A two-roll apparatus is used to explore experimentally the detailed fluid mechanics of meniscus roll coating in which inlets are starved and flow rates are small. Both forward and reverse modes of operation (with contra- and co-rotating rolls) are investigated using optical sectioning combined with dye injection and particle imaging techniques. That part of parameter space where meniscus coating occurs is identified by varying the roll separation and roll speeds and hence flow rate and capillary number.

Key features of the flow structures identified in the forward mode include two large eddies (each with saddle point, separatrix and sub-eddies), a primary fluid transfer jet and the existence of two critical flow rates associated with the switching-on of a second fluid transfer jet and the switching-off of the primary transfer jet followed by a change in the flow structure. In the reverse mode, the key features are a single large eddy consisting of two sub-eddies, a saddle point and separatrix, a primary fluid transfer jet and once again two critical flow rates. These correspond to (i) the switching-on of a secondary transfer jet and (ii) the disappearance of a saddle point at the nip resulting in the merger of the primary and secondary transfer jets.

Measurements of film thickness and meniscus location made over a range of speed ratios and capillary numbers are compared with theoretical predictions. A plate–roll apparatus is used to confirm the presence, for very small flow rates, of a sub-ambient, almost linear, pressure profile across the bead. Investigated also is the transition from inlet-starved to fully flooded roll coating as flow rate is increased and the changes in flow structure and pressure profile are observed.

1. Introduction

Essentially, a coating process is one whereby a thin film of liquid, of viscosity μ, density ρ and surface tension σ, is deposited onto a moving substrate which is subsequently dried or cooled to produce a solid film. Coating flows can be divided into two general categories, metered and pre-metered, according to whether the flow rate (and hence wet film thickness) is determined by the process or externally imposed. Examples of the former are fixed-gap flooded roll coating and knife coating, which are relatively inexpensive devices. Examples of the latter are meniscus roll coating, and also slide, slot and curtain coating which are capable of laying down more than one layer of fluid simultaneously.

The fluid mechanics of smooth, rigid roll coating has been investigated extensively both analytically (Schneider 1962; Greener & Middleman 1975, 1979; Savage 1982, 1984) and computationally (Coyle, Macosko & Scriven 1986, 1990*a*, *b*; Coyle 1992).

https://doi.org/10.1017/S0022112097007398 Published online by Cambridge University Press

However, each of these authors consider the classical roll-coating regime only in which the inlet is assumed to be fully flooded. If, on the other hand, the inlet is starved/ultra-starved the upstream meniscus plays a crucial role in determining the velocity and pressure fields. In practice these two coating regimes have quite different areas of application. The fully flooded process produces film thicknesses of the order of the gap size, whereas a starved/ultra-starved process produces superior quality, extremely thin films at line speeds of the order of a few tens of metres per minute.

One aim of this paper is to demonstrate the results of a systematic experimental investigation of the fluid mechanics of meniscus roll coating. The flow patterns revealed are seen to consist of large two-dimensional recirculations extending throughout the coating bead, in contrast to the quasi-unidirectional flow typical of inlet-flooded roll coating. In a companion paper, Gaskell *et al.* (1995*a*) present an analytical and computational investigation of forward-mode meniscus coating in which the various features of this flow regime are revealed and analysed. Richardson (1996) has recently completed a similar study of the reverse-roll problem – see also Richardson, Gaskell & Savage (1996) and Gaskell, Richardson & Savage (1998).

There have been few experimental investigations involving fundamental flow visualization studies of the internal fluid mechanics of roll coating flows. This is readily attributable to the difficult task of making observations and obtaining physical measurements of high-speed small-scale flows confined within restricted geometries. Also, it is arguable that the application, over the last decade or so, of powerful finite element techniques as a means of generating streamline flow patterns for a wide range of coating geometries (see for example Coyle *et al* 1986, 1990*a*, *b*; Christodoulou & Scriven 1989; Giavedoni & Saita 1992; Kistler & Scriven 1994) has contributed to the 'fall from grace' of experimental flow visualization studies. While such methods are capable of producing detailed information of the flow structure and have an obvious role to play in studying the behaviour of coating systems they are reliant on the provision of a good initial estimate for free-surface shapes and positions. They also require the boundary conditions which prevail at both static and dynamic wetting lines to be specified in an approximate sense since the physics is still a matter of some dispute (Dussan V. 1979; de Gennes 1985; Shikhmurzaev 1993; Blake, Clarke & Ruschak 1994). Similarly, the influence of surfactants (Schunk & Scriven 1997) and complex, or transient, rheologies (Glass & Prud'homme 1997) are also features of practical relevance that need to be modelled satisfactorily and incorporated accordingly.

Early experimental studies of the flow between contra-rotating rolls (Banks & Mills 1954; Miller & Myers 1958; Myers & Hoffman 1961; Floberg 1965) were motivated by similarities with the gear geometry investigated by Gatcombe (1945). The subsequent study of the flow in a plate–roll geometry performed by Pitts & Greiller (1961) and van de Bergh (1974) revealed the presence of a single eddy ahead of the downstream fluid–air interface. The former employed the crude flow visualization technique of introducing a series of small air bubbles into the flow and were the first to report the presence of downstream eddies in forward roll coating. The following year, Schneider (1962) reported an experimental and theoretical investigation of unequal roll speed coating. He performed a flow visualization study using transparent roll end dams and obtained streamline patterns and velocity profiles, for various roll speed ratios, by means of a painstaking manual frame-by-frame analysis of the associated flow field. Unfortunately, his discussion of variations in the dominant flow parameters is rather limited. The work of Benkreira, Edwards & Wilkinson (1981*a*, *b*), although extensive, considered in the main film thickness measurements with a view to determining an empirical relationship between the film split ratio and the roll speed ratio.

https://doi.org/10.1017/S0022112097007398 Published online by Cambridge University Press

In contrast there has been little experimental work published on reverse-mode roll coating despite its industrial importance – versatility, combined with its precision and speed capability, make it a commonly encountered coating technique for a wide range of products. Broughton, Egan & Sturken (1950) were the first to consider the transfer of a metered film on to a web and identified a linear relationship between its thickness and the roll separation. Ho & Holland (1978) and Benkreira, Edwards & Wilkinson (1982) presented useful data for this process over a very limited range of parameters, while Greener & Middleman (1981) reported data for a simple model coating system. Babchin, Clish & Wahren (1981), on the other hand, were concerned primarily with issues surrounding the stability of the process and the identification of 'safe operating windows' – those regions of parameter space where defect-free coatings can be obtained. The work of Coyle *et al.* (1990*b*) followed along much the same lines in trying to define 'experimental operability diagrams' in the context of cascade and the ribbing instability. However, as in the case of forward-mode roll coating, none of the above authors addressed the meniscus coating regime.

The art of good experimentation is illustrated clearly in the flow visualization study of slide coating made by Schweizer (1988). Using a combination of flow visualization techniques, including dye tracers and the hydrogen bubble method, he obtained lucid pictures of the associated flow field; in particular, his results revealed the presence of unexpected recirculations within the flow. Similarly, recent papers by Clarke (1995, 1996) vividly demonstrate the value of experiments in relation to understanding curtain coating processes. His work involved using a hydrogen bubble technique, similar to that reported by Schweizer (1988), to carry out a detailed investigation of flow structure in the heel of a curtain coater and to describe its evolution as a function of capillary number and flow rate. See also the work of Wicks *et al.* (1995) relating to the use of particle tracking as a means of exploring the flow topology present in the downstream region of a flooded twin-roll coating device – of particular interest is the disjoint eddy structure which results as a consequence of any type of asymmetry introduced into the system.

The flow investigated here is even more demanding experimentally and progress has only been made possible by recent advances in state-of-the-art video systems and image processing technology. Malone (1992) was the first to employ such techniques to explore the flow in the nip region of a starved fixed-gap forward roll coater and to succeed in unravelling the underlying macroscopic flow structure. Decré, Gailly & Buchlin (1995) used similar techniques to carry out a systematic experimental investigation for the case of asymmetric forward roll coating with the goal of measuring downstream meniscus profiles and location, via a laser sheet technique, together with the total flow rate and its distribution on the rolls. The coating fluid was doped with a fluorescent medium for this purpose. Their results are of considerable interest but it is difficult to discern from them which is the dominant asymmetry since their apparatus consisted of two rolls of unequal radius inclined at an angle of roughly 45° to each other, with fluid entering the coating bead via the smaller of the two rolls. In a recent paper, Gaskell, Savage & Walker (1998) have carried out a complementary investigation but with the gravitational and geometric asymmetries removed. They consider the case of rolls placed side-by-side, half submerged in a bath of liquid. A number of interesting results emerge, the key one being that under certain conditions the free surface collapses into the nip.

In order to examine the flow in question a precision, small-scale experimental apparatus, retaining all the important features of its industrial counterpart, was designed as described in §2. The practical difficulties of investigating a fluid bead located

https://doi.org/10.1017/S0022112097007398 Published online by Cambridge University Press

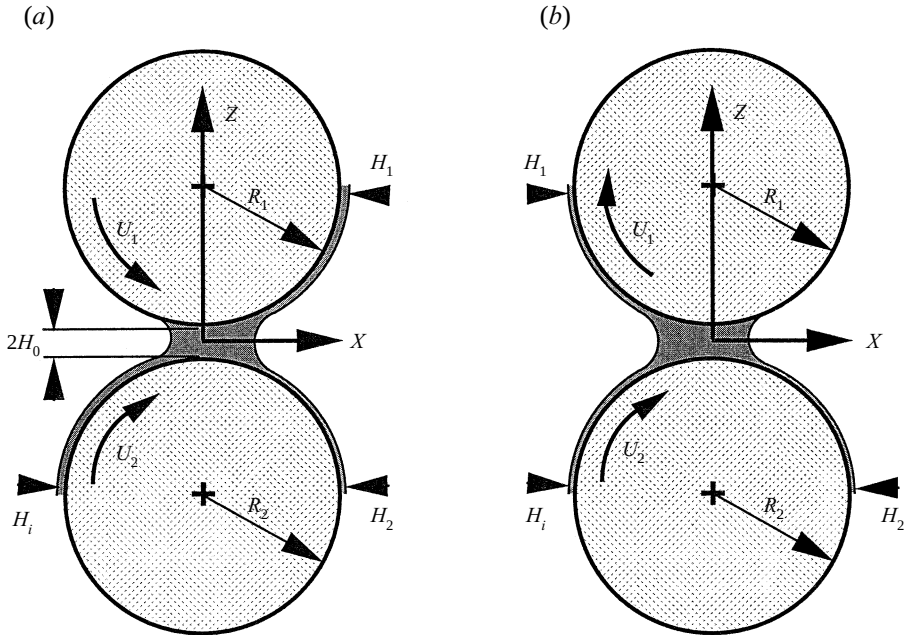


FIGURE 1. Cross-section showing modes of operation for rolls mounted one above the other: (*a*) forward; (*b*) reverse.

between two moving rolls and consisting of two free surfaces, a dynamic wetting line and small characteristic dimensions are discussed in detail. A full account is given also of the flow visualization methods employed and the techniques used to record and analyse the flow. Considerable reliance is placed upon the use of particle imaging together with processing images captured from video recordings. These techniques are applied to a series of experiments focusing on the novel flow field associated with starved/ultra-starved forward and reverse roll coating and the transformation to the classical regime as flow rate is increased. Film thickness measurements, meniscus locations and critical flow rates are presented, and also typical pressure profiles for a plate–roll apparatus.

The methods described here need not be restricted to the investigation of roll coating systems and have potential application for the study of other lubrication-type flows.

1.1. *Description of coating regimes*

In forward roll coating the two rolls contra-rotate, figure 1(*a*), whereas in the reverse case they co-rotate, figure 1(*b*). Rolls of radius R_1 and R_2 moving with peripheral speeds U_1 and U_2 respectively, are located one above the other. Liquid, picked-up from a coating bath by the action of viscous lifting, is transferred from the lower, applicator roll, to the web on the upper roll in one of two possible flow regimes, classical or meniscus, for which the inlet or feed condition is either fully flooded or starved/ultra-starved.

For a flooded inlet it is convenient to refer to the flux per unit axial length, Q, in the following non-dimensional form

$$\lambda = \frac{Q}{2H_0U},$$

https://doi.org/10.1017/S0022112097007398 Published online by Cambridge University Press

where $U = (|U_1| + U_2)/2$ and H_0 is the minimum semi-gap width. However, in the case of starved/ultra-starved inlets a more natural measure of the non-dimensional flow rate (Gaskell *et al.* 1995*a*) is given by

$$\lambda_i = \frac{H_i}{2H_0}, \tag{1.1}$$

where H_i is the inlet film thickness and λ_i is related to λ by the expression $\lambda_i = \lambda(1 + |S|)/2$. Here $S = U_1/U_2$, the roll speed ratio.

In the meniscus coating regime the upstream meniscus is found to lie close to the nip, giving a compact fluid domain referred to as the coating or fluid 'bead'. In fact this meniscus is found to play a crucial role in generating a sub-ambient pressure field in which capillary and hydrodynamic pressures are of the same order of magnitude. If $Ca = U\mu/\sigma$ is the capillary number and $R = 2(R_1^{-1} + R_2^{-1})^{-1}$ the effective roll radius, the meniscus coating regime is located in that part of parameter space where modified capillary numbers are small, that is where

$$Ca\left(\frac{R}{H_o}\right)^{1/2} \leqslant 0.15. \tag{1.2}$$

This is in contrast to the classical coating regime where the upstream meniscus is located far upstream of the nip and its influence on both the flow and pressure field is negligible. Also, hydrodynamic forces, generated in a converging gap through the action of viscosity, are much greater than capillary pressure at a meniscus. Later it will be found convenient to quote a capillary number based on the lower-roll speed, namely $Ca_2 = \mu U_2/\sigma$, with $Ca = Ca_2(1 + |S|)/2$.

2. Experimental apparatus and method

2.1. *Description of apparatus*

The pilot roll coating apparatus and supporting equipment are shown schematically in figures 2 and 3. The apparatus consists of two independently driven horizontal-axis rolls, cantilever-mounted on a steel base, allowing easy access to the nip region. The lower, applicator roll is partially submerged in a bath of liquid. A precision slide and micrometer enable the upper roll to move vertically and so allow changes to the gap separating the rolls. The 100 mm wide stainless steel rolls are precision ground to a diameter of 50.48 mm with a surface roughness R_a value of 0.4 μm. The combined roll run-out (eccentricity) is less than 3 μm, giving very stable meniscus locations even for the smallest of roll separations. Each roll rotates within precision bearings and is driven by a permanent magnet DC motor through a 30:1 gearbox. These motors have the advantage of low cost, but also have the drawback of not being absolutely steady at low speeds. This could be overcome by installing costly feedback control, but was considered unnecessary since most of the experiments were performed in the moderate to high speed ranges. The motor speeds and their peak-to-peak deviations are monitored on a PC and controlled via two stabilized power supplies, giving roll surface speeds and capillary numbers in the range $U \in (9.3 \times 10^{-3}, 2.8 \times 10^{-1})$ m s^{-1} and $Ca_2 \in (2.20 \times 10^{-3}, 1.16 \times 10^{-1})$, respectively.

The bath and reservoir system requires about 5 litres of liquid. Two light oils were used with typical properties shown in table 1, which are subject to temperature variation and degradation and hence measurements are necessary before and after any set of experiments. Aqueous solutions are avoided to prevent rusting of steel

https://doi.org/10.1017/S0022112097007398 Published online by Cambridge University Press

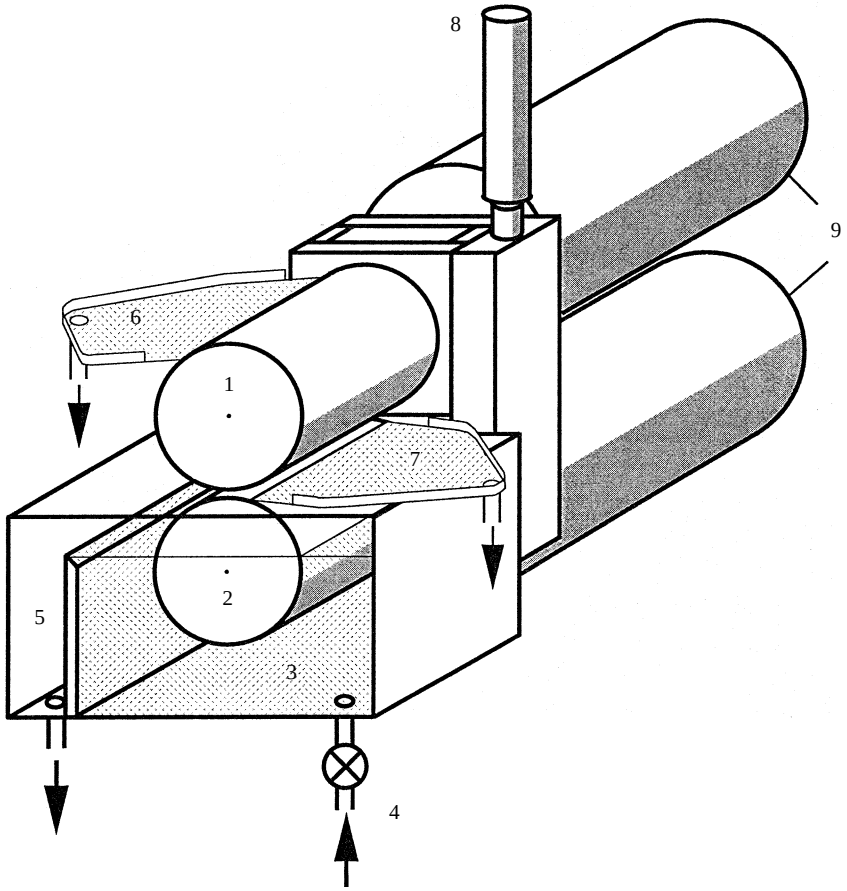


FIGURE 2. Schematic showing the main features of the experimental apparatus: (1) upper roll; (2) lower roll; (3) coating bath; (4) 1/4 turn valve; (5) weir; (6) and (7) wipers; (8) micrometer; (9) motors.

	Oil 1	Oil 2
Surface tension	$\sigma = 2.85 \times 10^{-2}$ N m^{-1}	$\sigma = 2.98 \times 10^{-2}$ N m^{-1}
Density	$\rho = 842$ kg m^{-3}	$\rho = 834$ kg m^{-3}
Dynamic viscosity	$\mu = 11.79 \times 10^{-3}$ Pa s at $T = 25.0\,^{\circ}$C	$\mu = 6.75 \times 10^{-3}$ Pa s at $T = 25.0\,^{\circ}$C

TABLE 1. Typical properties of the oils used in the experiments

components and to minimize surface tension gradient effects from the addition of dyed tracer liquid. The entire apparatus is kept in a clean environment under constant temperature conditions, monitored via a bath-mounted thermometer. This is important since a temperature rise of one degree causes approximately a 4% decrease in viscosity at room temperature.

A 5 litre capacity, spring-mounted tank is used to supply a virtually steady flow to the bath, regulated by a quarter-turn valve. The springs are chosen so that the liquid level within the tank remains a fixed distance above the bath, regardless of the volume of oil in the tank. A syphon is used to add or remove liquid while enabling

https://doi.org/10.1017/S0022112097007398 Published online by Cambridge University Press

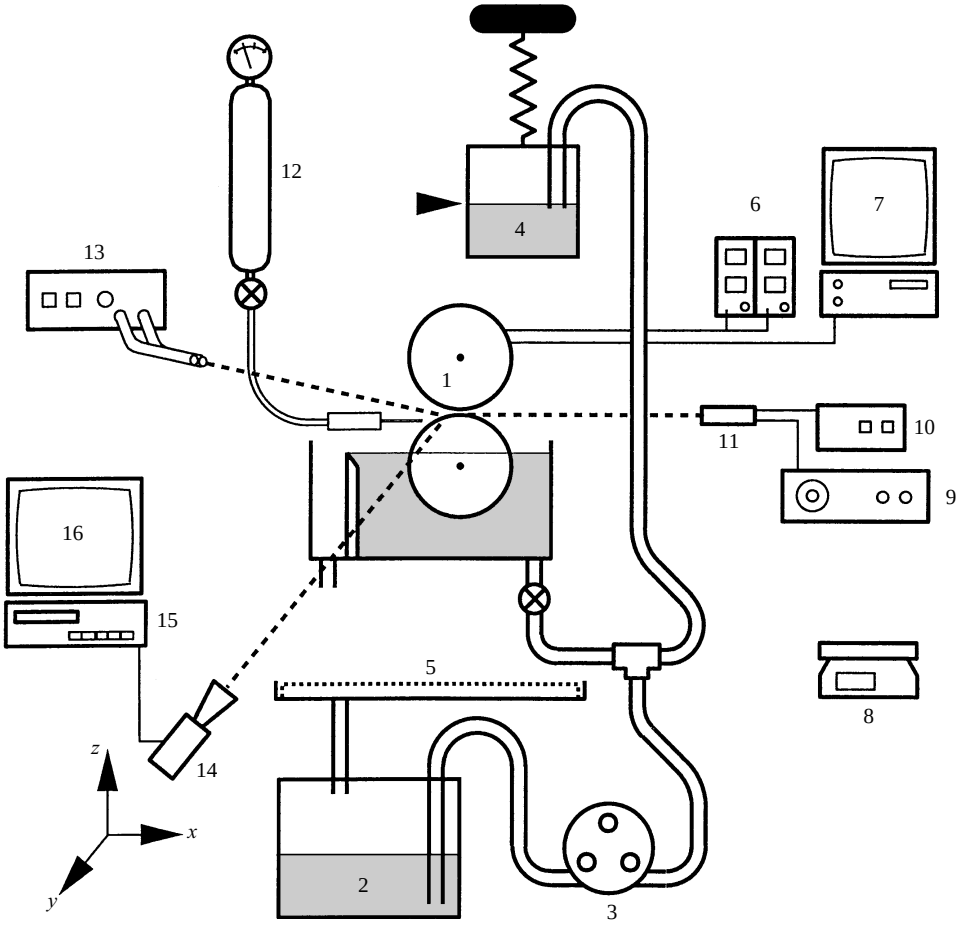


FIGURE 3. Schematic of the experimental layout: (1) two-roll apparatus; (2) coating bath; (3) pump; (4) upper reservoir; (5) drip-tray; (6) DC power supplies; (7) PC; (8) digital scale; (9) wave form generator; (10) inter-locked power supply; (11) diode laser; (12) pressurized dye tank; (13) fibre optic light source; (14) microscope and video camera; (15) video recorder; (16) monitor.

vertical movement of the tank. A peristaltic pump allows both the bath and the tank to be filled or emptied as required. A drip tray collects all outflow from the bath and wipers (see below) which serve two purposes: (i) the measurement of flow rates; (ii) when in contact with the upper roll they mimic the action of a web.

An overflow weir mounted in the bath keeps the fluid level constant to within 1 mm, ensuring repeatability of the flow rate supplied by the lower roll. Flow rate control is achieved by varying the lower roll speed and by replacing the weir with one of a different height. Two weirs are used, one 58 mm high and the other 26 mm high. The first produces comparatively thick inlet films while the second results in a 'kissing' contact between roll and fluid, minimizing churning of the bath and any associated rise in oil temperature over a period of several hours. The data for film thickness supplied by the lower roll, figure 4, may be curve-fitted with functions of the form

$$D_i = A\,Ca_2^B, \tag{2.1}$$

where $D_i = H_i(\rho g/\sigma)^{1/2}$ represents a non-dimensional film thickness. For the 58 mm

https://doi.org/10.1017/S0022112097007398 Published online by Cambridge University Press

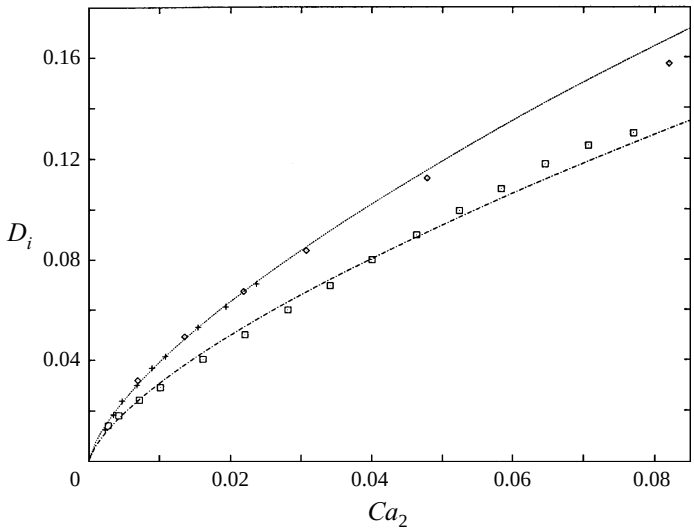


FIGURE 4. Typical inlet film thickness data as functions of Ca_2 (lower roll speed) and weir height: upper curve, 58 mm weir; ◇, Oil 1; + Oil 2; lower curve, 26 mm weir; □, Oil 1.

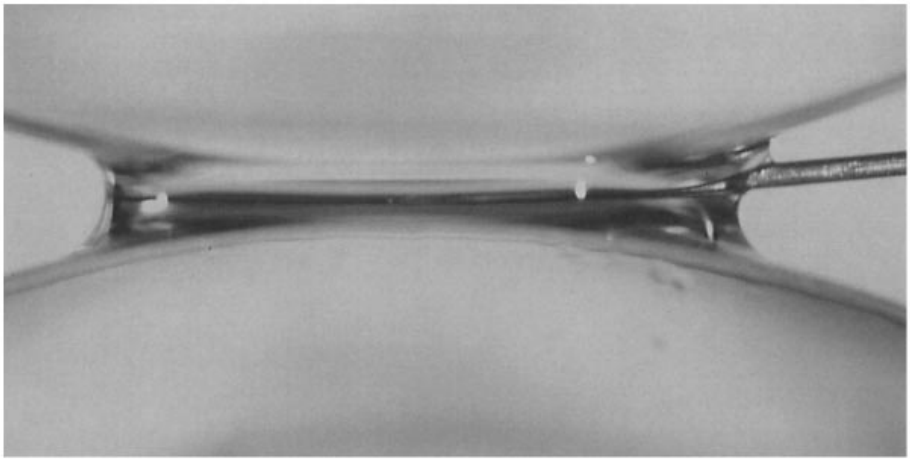
weir the coefficients are $A = 0.94$, $B = 0.69$ and for the 26 mm weir $A = 0.74$, $B = 0.69$. These data compare well with film thicknesses predicted by viscous lifting theory, Innes (1993). It is interesting to note also that equation (2.1) is of a similar form to that suggested by Landau & Levich (1942) for the associated drag-out problem.

Flow rates for the rolls are measured by wiping them, along their entire length, with a twin polyethylene blade system and collecting the liquid over a fixed timed interval. The uniformity of the incoming film on the applicator roll was assessed visually using a microscope at various stations along its length. The twin-blade system was found to leave a residual film less than 0.2 μm thick adhering to the rolls, estimated from blotting tests with a paper towel. This gives wiping efficiencies exceeding 99% for films of more than 20 μm thickness. Although the upper roll surface is not completely dry, it nevertheless serves as an adequate approximation to an incoming dry substrate for the purpose of determining flow rates. Similarly, observed meniscus locations may differ compared with those for a completely dry roll due to any corresponding effect on the dynamic contact angle subtended at the wetting line. Unfortunately, it was not possible to quantify such effects with the apparatus to hand.

A Perspex plate is mounted flush against the roll faces at each end to minimize axial leakage from the coating bead and to create an undistorted viewing window. The coating bead would otherwise have a curved surface at the roll ends which would act as a lens, obscuring details of the internal flow structure. Figure 5 serves to illustrate the improved visibility obtained by installing a window – a hypodermic needle inserted into the nip can only be seen clearly when the end plates are *in situ*. A monocular 0.7–4.5× zoom microscope assembly (Meiji Techno Company) with 0.5× magnifier lens and video camera allows viewing in a direction parallel to the roll axes. The whole assembly is mounted on a 3-axis translating table with micrometers for X–Z positioning to within 20 μm. Movement along the Y-axis is used for focusing the microscope. The optimum viewing depth into the bead is affected by the roll separation; a depth in the range 5–7 mm was found to be sufficient, for the gap settings used, to guarantee a flow field essentially two-dimensional in a cross-sectional

https://doi.org/10.1017/S0022112097007398 Published online by Cambridge University Press

(*a*)



(*b*)

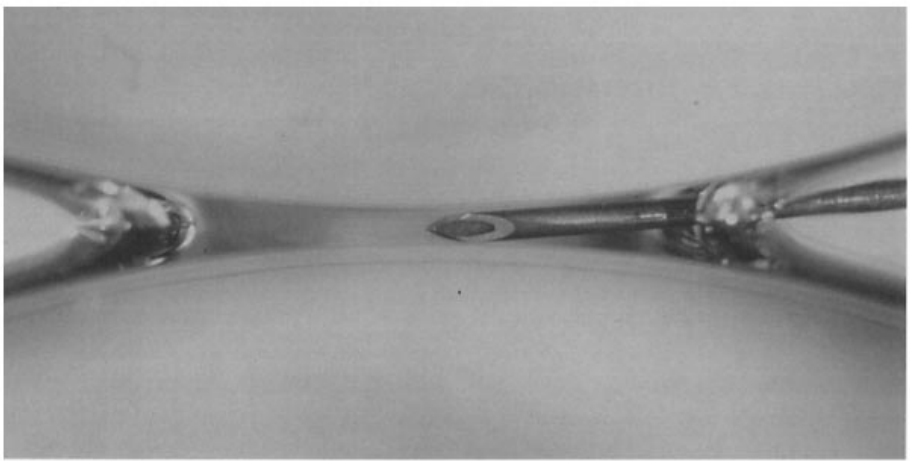


FIGURE 5. View of a needle inserted into the coating bead: (*a*) with no end plate *in situ*; (*b*) with an end plate present.

plane – the roll edges are slightly out of focus but the meniscus appears sharp. Note that if the plane of focus is too close to the roll ends the flow field will be affected by the presence of the end plate.

Two optical fibre light guides (Olympus Highlight 3000) mounted at the bearing housing end of the rolls are used to illuminate the bead by means of total internal reflection, leaving the rest of the field of view dark. This lighting arrangement eliminates optical reflections from the meniscus which wets the end plate, allowing high-contrast images of the liquid/air interface to be obtained. Alternatively, a diode laser is used to provide optical sectioning of the flow field. Video records of the experiments are made using S-VHS video equipment. Two video cameras are employed, one for colour information (Panasonic WV-KS152E), the other for black and white low-light conditions (Panasonic 0.08 lux model WV-BP310B), with laser illumination. The second camera allows high-contrast images to be obtained without the need for a light intensifier. A graticule mounted within the microscope enables a grid to be

https://doi.org/10.1017/S0022112097007398 Published online by Cambridge University Press

superimposed on the video images for measurement purposes. An external 1 mm reference scale is used to calibrate the superimposed grid for accurate scaling of flow features.

2.2. *Experimental method*

Essentially four types of experiment were performed for forward and reverse roll coating: (i) flow visualization; (ii) film thickness measurement; (iii) meniscus location; (iv) pressure field determination. In the first, the flow visualization techniques described below were used to validate experimentally the existence of fluid transfer jets and the eddy structures present within the coating bead. The applicator roll speed U_2 was fixed and the upper roll speed U_1 (or S, the roll speed ratio) was varied until a critical event was observed. The inlet flow rate was then measured to obtain λ_i. Two techniques, dye injection and particle imaging, were used to reveal the flow structures. These complemented each other by allowing both transfer jets and recirculation zones to be seen clearly.

In the second series of experiments, measurements of film thickness were made by means of the wipe-off technique described earlier. Flow rate data were obtained by wiping each roll, of length L, and collecting liquid mass, M_j, over a measured time interval, T_j, typically five minutes. A digital balance was used to determine the collected mass to within 2×10^{-4} kg, with a minimum mass of 10^{-2} kg (1.2×10^{-2} l of oil). Volume flow rates per unit length, Q_j, were then obtained from the relationship

$$Q_j = \frac{M_j}{\rho T_j L}, \quad j = 1, 2. \tag{2.2}$$

The film thickness, H_j, on each roll can then be estimated under the assumption of fully developed flow as

$$H_j = \frac{Q_j}{U_j}, \quad j = 1, 2. \tag{2.3}$$

Simultaneous video recordings made during the wipe-off experiments enabled the upstream and downstream meniscus positions, X_u and X_d, to be located relative to the nip – back lighting and a superimposed graticule were used for this purpose. Of the order of 200 individual experiments were carried out with data acquired for various roll speeds U_1, U_2, and hence speed ratios S, in the range $S \in \pm(0.167, 33.0)$ with gap ratios of $R/H_0 = 100$, 200 and 400, giving full coverage of coating regimes from ultra-starved to fully flooded.

Finally, the simple plate–roll apparatus described in §5 was used to investigate the pressure field in the nip region. The apparatus is representative of the limiting case of a stationary upper roll of infinite radius.

2.2.1. *Dye injection*

The existence of flow structures can be highlighted relatively easily by injecting coloured or dyed liquid through a hypodermic needle into the upstream flow and viewing its passage through the nip. The dye trace can be either continuous or pulsed. A small tank pressurized to about 100 kPa is used to force dyed liquid, the same as that used in the experiments, through the injection line and needle (bore 200 μm). A blue powder dye (grasol blue, or solvent blue 27) was found to dissolve well in oil, giving excellent contrast with only minimal changes to the liquid properties. The dye appears brighter than the surrounding fluid when illuminated by the laser and darker than the fluid when the bead is back-lit. Only the fluid transfer jets within the flow can be seen directly since the dye does not easily diffuse into the closed eddies.

https://doi.org/10.1017/S0022112097007398 Published online by Cambridge University Press

Since dye injection involves adding a very small quantity of liquid to the existing flow field far upstream, the local inlet flux is increased only slightly. Changes to the meniscus locations are indiscernible and so the dye trace patterns can be considered representative of the flow patterns existing in a cross-sectional plane of the unperturbed flow.

2.2.2. *Particle imaging*

The flow details within the eddies are observed by means of 8 μm diameter hollow glass spheres (supplied by Potters Industries Inc.) seeded throughout the liquid. These are preferred to solid glass particles since their density is much closer to that of the liquid, rendering them neutrally buoyant. The hydrogen bubble technique employed by Schweizer (1988) and Clarke (1995, 1996) is not practical for a number of reasons: (i) the liquid used is not electrically conductive; (ii) both roll surfaces are moving; (iii) the coating bead is prohibitively small. The concentration of particles in the flow is typically less than 0.1% by volume to maintain optical clarity for recording purposes and to avoid detectable changes to the liquid properties.

A low-power 19 mW, 680 nm (red) pulsed diode laser is used to illuminate a 1 mm thick slice through the flow field perpendicular to the viewing direction, Clarke (1995). The laser is modulated via a variable dwell wave form generator enabling its power to be varied and frame-to-frame tracking of single particles. The device was positioned on the downstream side of the nip resulting in only a marginal reduction in illumination of the upstream flow due to attenuation of the laser beam. The resulting particle tracks, with typically several thousand particles visible at any one time, were recorded with the black-and-white video camera described earlier. These particle concentrations are obtained by dropping dry particles onto the inlet film, giving intense images that reveal the internal flow structures. For lower concentrations, the flow structures cannot be discerned from single images. No attempt was made to track the motion of individual particles in order to determine velocities within the flow, although Decré (1994) has shown this to be possible provided a sufficiently powerful laser and requisite software is available.

The final component of the particle imaging system is the capture of single or sequential images from video recordings and their subsequent manipulation to discern useful flow information. A Silicon Graphics Indigo 2 workstation with video board was used to produce the majority of the figures presented in subsequent sections. The quality of the experiments was sufficiently good that only minor adjustments to control the contrast were required. However, the workstation has powerful facilities for editing the image, image enhancement and for the addition of successive images to highlight flow structures. In addition, arrows have been super-imposed on some images to assist the reader and to convey the effect of motion present on the video recordings. Also, where necessary, arcs of circles have been used to highlight the edge of the rolls and cancel out the presence of reflections on the air side of the meniscus profiles. Considerable care and attention to detail was required in performing these tasks, Schweizer (1996, 1997).

3. Forward roll coating

Topologically forward roll coating is the most interesting mode of operation with its rich variety of flow structures, Gaskell *et al.* (1995*b*). Beginning with the ultra-starved regime, the flow patterns for the transition to fully flooded coating are illustrated.

https://doi.org/10.1017/S0022112097007398 Published online by Cambridge University Press

Following this, the experimental film thickness data and meniscus locations are compared with the theoretical predictions of Gaskell *et al.* (1995*a*).

3.1. *Flow structures and fluid transfer jets*

The characteristic features of the meniscus coating regime are large eddy structures distributed throughout the coating bead together with the transfer of liquid from one roll to the other by means of a single or two fluid transfer jets, Gaskell *et al* (1995*a*). When the flux $\lambda_i \in (0, \lambda_{is})$ there is only one, primary transfer jet present, as illustrated in the sequence of dye traces shown in figure 6 for the case $S = 0.7$. It can be seen that the incoming flux (lower left corner) travels the length of the bead, figure 6(*a*), to the downstream meniscus where it splits; a part then continues with the lower roll, leaving the bead, while the remainder turns to flow in the reverse direction between two large contra-rotating eddies, figure 6(*b*). The jet turns once again, at the upstream meniscus, to flow the length of the bead and emerge attached to the upper roll surface, figure 6(*c*). The times quoted were measured from the instant the primary transfer jet entered the bead.

A particle image of the same flow field, figure 7, serves to reveal the existence of two sub-eddies within each of the large contra-rotating eddies. A finite element solution (see Gaskell *et al.* 1995*b*) for the same flow conditions, figure 8, shows the corresponding streamline pattern. The bead is found to contain five free-surface saddle points, two internal saddle points and four centres with each pair of sub-eddies contained within a 'figure-of-eight' or separatrix, the saddle point of which is located at the nip.

As the inlet flux increases, the strength of the primary transfer jet increases causing the contra-rotating eddies to diminish in size. When the flux exceeds a critical value λ_{is} the presence of a secondary transfer jet is observed, whose strength increases with λ_i and which takes a path between the two lower sub-eddies. This can be seen from the dye trace in figure 9, where part of the inlet flow separates from the primary transfer jet to form this secondary jet. The broken vertical lines in figures 9–12 indicate the minimum gap (nip) position.

As the flux increases further, the secondary transfer jet continues to grow in strength at the expense of the primary one. A second critical flux value, λ_{ip}, is soon reached at which point the primary transfer jet disappears. This point is significant for two reasons: (i) it signifies the end of the meniscus coating regime; (ii) it marks the point at which the fluid transfer to the upper roll is entirely by way of the secondary transfer jet – see figure 10. The strength of the secondary transfer jet as seen from this figure was sufficient to cause the lower upstream eddy to vanish completely.

The flux value, λ_{ip}, at which the primary transfer jet vanishes as the saddle points in the nip come together precedes the emergence of a region of quasi-unidirectional flow at the nip as λ_i increases further. The extent of this region continues to increases with λ_i, figure 11, and is bounded to the right by two eddies which form the downstream recirculation region. This process continues until the inlet is fully flooded, $\lambda_i = \lambda_{i(max)}$, and an upstream bank is established – see figure 12 – entering what is referred to as the classical roll coating regime.

The critical flow rates λ_{is} and λ_{ip} are dependent upon the speed ratio, S. Experimentally they are difficult to observe and hence pinpoint precisely since the switching-on/switching-off of a transfer jet implies zero flow rate through it, whereas dye can only be used to distinguish jets to within a finite flow rate. Observing the switching-off of the primary transfer jet is particularly difficult since over time dye diffuses into the perimeter of the lower eddy and can give the false impression that

https://doi.org/10.1017/S0022112097007398 Published online by Cambridge University Press

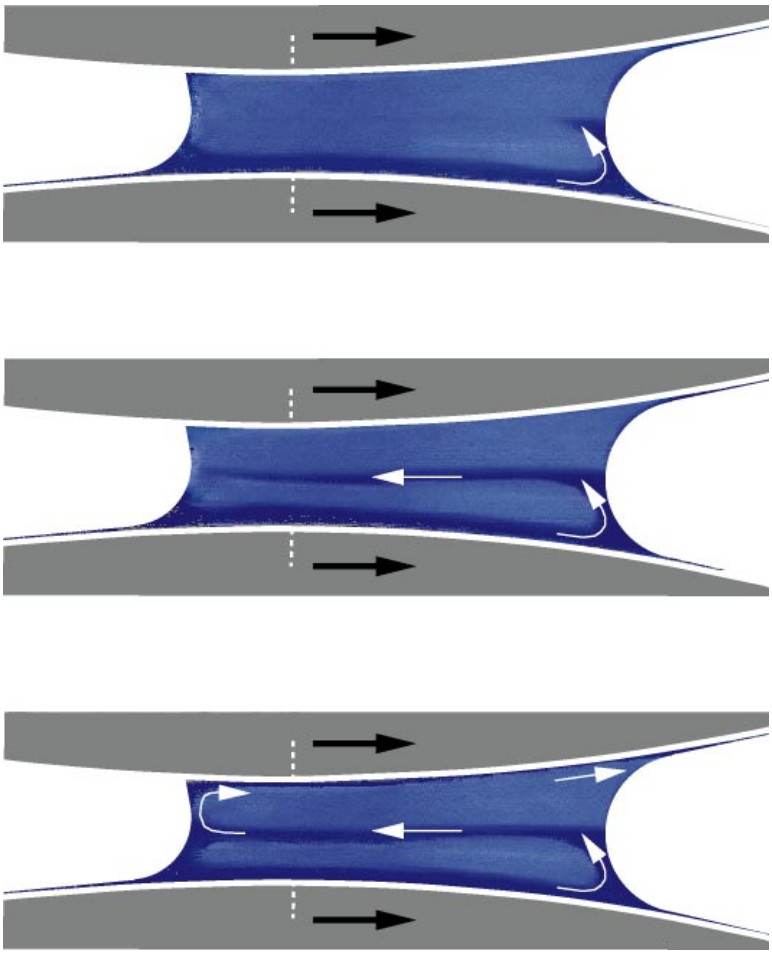


FIGURE 6. A sequence of dye traces showing the path of the primary transfer jet through the bead for forward-mode meniscus coating ($R/H_0 = 68$, $S = 0.7$, $\lambda_i = 0.076$, $Ca_2 = 8.0 \times 10^{-3}$): time $t =$ (*a*) 1 s, (*b*) 2 s, (*c*) 3 s from when the primary transfer jet first enters the bead. The broken vertical line indicates the minimum gap (nip) position.

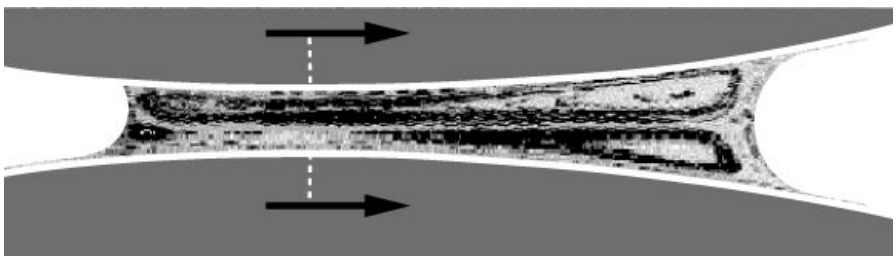


FIGURE 7. Laser illuminated particles for the case of forward-mode meniscus roll coating: $R/H_0 = 100$, $S = 1.0$, $\lambda_i = 0.048$, $Ca_2 = 2.3 \times 10^{-3}$. The image, shown in negative form, is made up from eight frames, grabbed sequentially and added together electronically. The broken vertical line indicates the minimum gap (nip) position.

https://doi.org/10.1017/S0022112097007398 Published online by Cambridge University Press

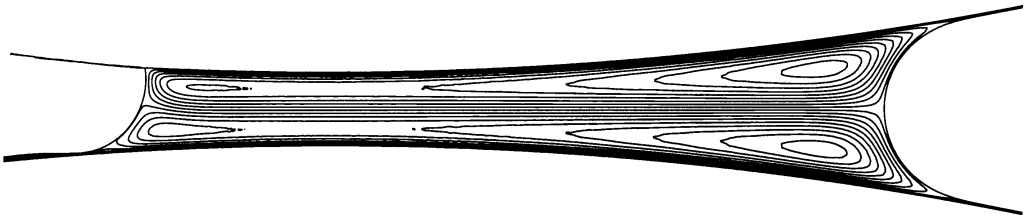


FIGURE 8. Finite element solution corresponding to the flow field shown in figure 7.

there is still a jet present between the lower and upper eddies. Figure 13 shows experimental flow rate data for λ_{is} as a function of speed ratio; included also are schematics of the flow structures present. The 'observability threshold' and 'pseudo-jet' effects explain why the data are shifted below the theoretically predicted values, Gaskell *et al* (1995*a*), for λ_{is}:

$$\lambda_{is} = \tfrac{1}{9}\left(3 + 2S - 2(S^2 + 3S)^{1/2}\right). \tag{3.1}$$

3.2. *Film thickness measurements*

In forward-mode meniscus coating, the effect of speed ratio, S, is to cause asymmetric film splitting resulting in films of unequal thicknesses attached to the two rolls. For $R/H_0 = 100$, $Ca_2 = 1.6 \times 10^{-2}$ and $\lambda_i = 0.141$ figure 14 shows data for both H_1 and H_2 as S is increased from 0 to 1.2. Also included are the theoretical curves, as predicted by Gaskell *et al.* (1995*a*), for small capillary numbers with the effect of gravity assumed to be negligible and $\lambda_i \in (0, \lambda_{ip})$. They also predicted a two-thirds power law for the film split ratio

$$\frac{H_1}{H_2} = S^{2/3}. \tag{3.2}$$

Figure 15(*a*) shows experimental data for several R/H_0 ratios, which consistently fall on a curve that lies below that given by equation (3.2). A simple model, derived in the Appendix, is sufficient to show that this discrepancy is due to the effect of gravity at the downstream meniscus. When the experimental data are adjusted to remove the effect of gravity, agreement with theory is much closer, figure 15(*b*).

3.3. *Meniscus location and bead break*

The coating bead is bounded by two free surfaces (an upstream and a downstream meniscus) the locations of which, $\bar{x} = X/(2RH_0)^{1/2}$, are sensitive to variations in Ca_2, S and R/H_0. Gaskell *et al.* (1995*a*) derived a relationship for the position of the downstream meniscus $\bar{d} = X_d/(2RH_0)^{1/2}$ in terms of λ_i, S and $Ca = Ca_2(1 + |S|)/2$. This relationship (equation (3.22) in their paper) contains an error, due to $S^{5/3}$ in the denominator being written as $S^{2/3}$, and should read

$$1 + \bar{d}^2 = \frac{2\lambda_i}{1.34}\frac{(\frac{1}{2}(1+S))^{2/3}}{(Ca)^{2/3}[1 + S^{5/3}]} = \frac{2\lambda_i}{1.34(Ca_2)^{2/3}[1 + S^{5/3}]}.$$

For a given flow rate this equation predicts a dependence of $\bar{d}$ on $(Ca_2)[1 + S^{5/3}]^{3/2}$ as illustrated in figure 16 where meniscus location data are shown for three gap settings, $R/H_0 = 100$, 200 and 400, with flow rate kept constant, $\lambda_i = 0.16$. In each case several features can be observed as the upper roll speed only (and hence S) is increased: (i) the width of the bead contracts; (ii) the downstream meniscus location data appear to follow approximately the same curve as that

https://doi.org/10.1017/S0022112097007398 Published online by Cambridge University Press

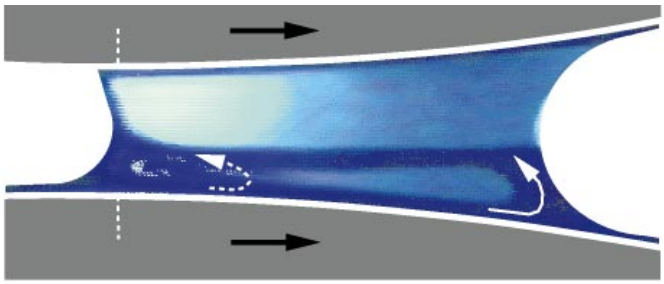


FIGURE 9. Dye trace showing the presence of a secondary transfer jet in the bead for the case of forward-mode meniscus coating ($R/H_0 = 68,\ S = 1.3,\ \lambda_i = 0.096,\ Ca_2 = 9.7 \times 10^{-3}$). The primary transfer jet is also present following a similar path as that shown in figure 6.

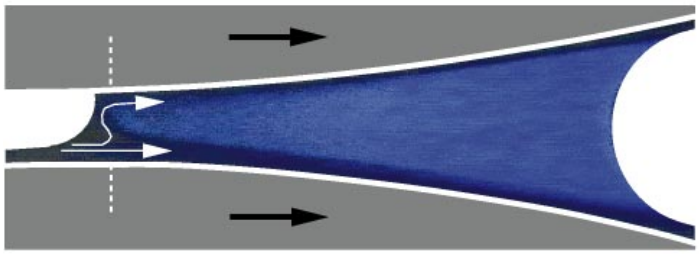


FIGURE 10. Dye trace showing the absence of a primary transfer jet and that transfer of fluid to the upper roll is entirely by means of the secondary transfer jet ($R/H_0 = 100,\ S = 1.0,\ \lambda_i = 0.29,\ Ca_2 = 2.78 \times 10^{-2}$).

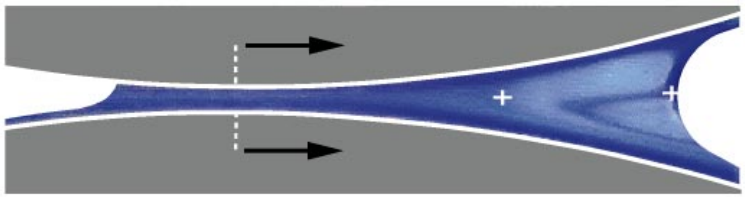


FIGURE 11. Moderately starved forward roll coating with no upstream bank; the approximate positions of the two downstream saddle points are indicated by + ($R/H_0 = 200,\ S = 0.67,\ \lambda_i = 0.89,\ Ca_2 = 5.66 \times 10^{-2}$).

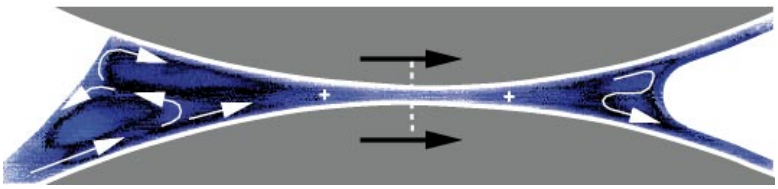


FIGURE 12. 'Fully' flooded forward roll coating with an upstream bank and two saddle points (indicated by +) marking the onset of regions of recirculating flow ($R/H_0 = 200,\ S = 0.69,\ \lambda_i = 1.08,\ Ca_2 = 9.83 \times 10^{-2}$). Flow-back occurs at the inlet since only part of the incoming flow can pass through the nip.

https://doi.org/10.1017/S0022112097007398 Published online by Cambridge University Press

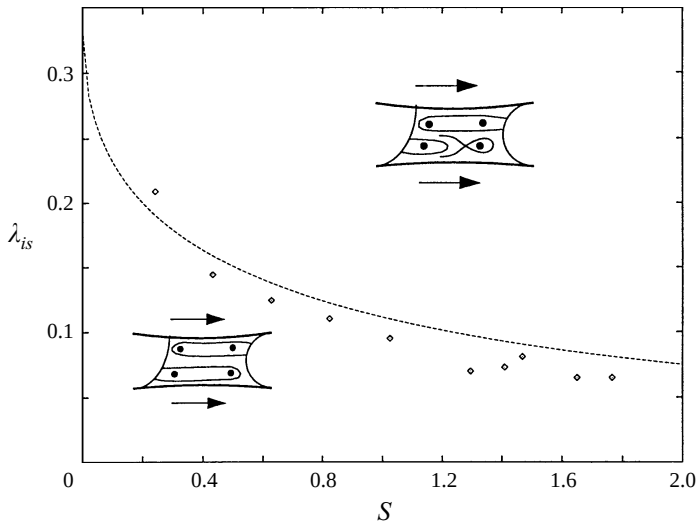


FIGURE 13. Critical flow rate λ_{is} plotted against S for the switching-on/-off of the secondary transfer jet in the case of forward mode meniscus coating: - - - -, theoretical curve (equation (3.1)); $\diamond$, experimental data.

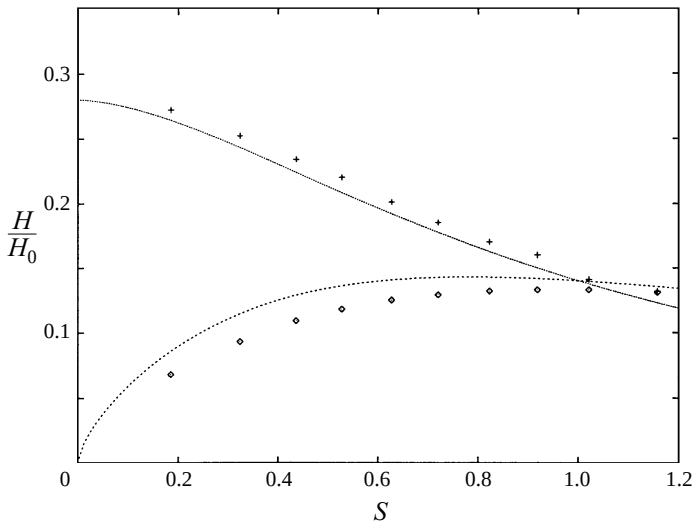


FIGURE 14. Film thickness data $\diamond$, $+$ and theoretical predictions - - - - - , ——— for H_1/H_0, H_2/H_0 respectively as functions of S for the case of forward-mode meniscus coating ($R/H_0 = 100$, $Ca_2 = 1.6 \times 10^{-2}$, $\lambda_i = 0.141$).

predicted by theory, Gaskell *et al.* (1995*a*) – any deviations, particularly at small values of S, are due to the effect of gravity; (iii) the upstream meniscus depends on R/H_0 – in fact theory predicts a dependence on the modified capillary number, $Ca(R/H_0)^{1/2}$; (iv) the upstream meniscus approaches the nip and there is a small range of S values over which the bead is stable and lies entirely downstream of the nip; (v) bead-break arises when the two menisci come together.

https://doi.org/10.1017/S0022112097007398 Published online by Cambridge University Press

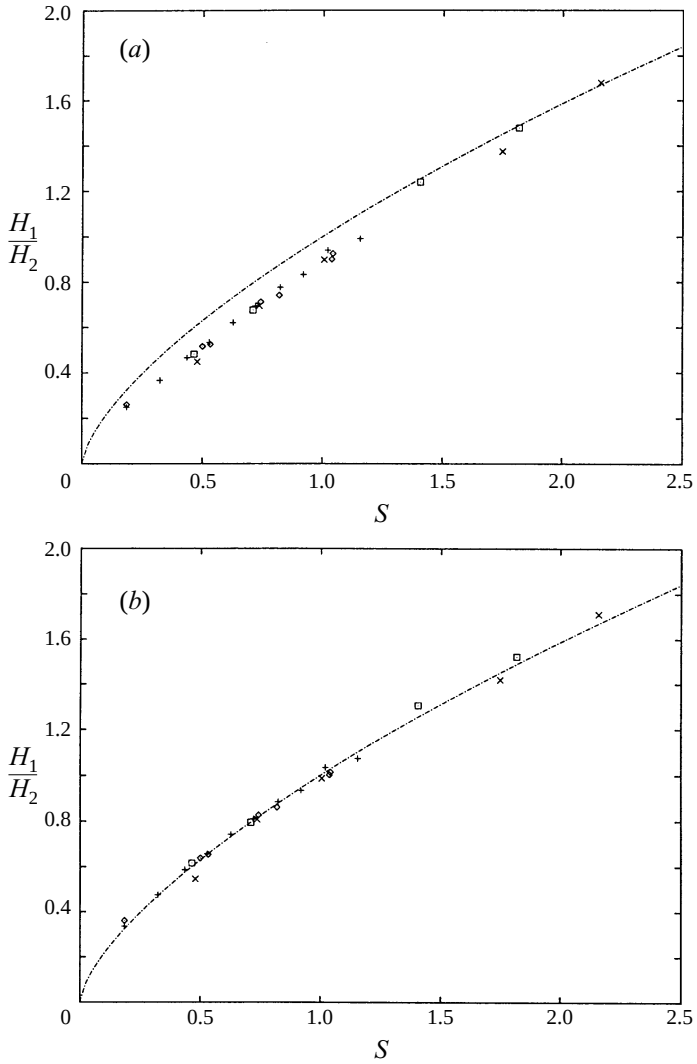


FIGURE 15. Forward-mode meniscus coating; a comparison of theoretical (equation (3.2)) and measured film split ratios (*a*) actual, (*b*) adjusted for the effect of gravity ($\diamond$, $R/H_0 = 100$; $+$, $R/H_0 = 200$; $\square$, $R/H_0 = 400$; $\times$, $R/H_0 = 800$).

4. Reverse roll coating

Whereas forward roll coating has received much attention, both theoretical and experimental, it is the reverse mode which is more flexible, robust and hence of considerable practical importance, Coyle (1992). The two modes have their similarities and differences. In reverse-mode roll coating the rolls co-rotate and the fluid bead is characterized by a single, large eddy structure, figure 17. However, fluid transfer from the applicator roll to the upper roll is achieved as in the forward mode – by means of primary and secondary transfer jets.

4.1. *Flow structures and fluid transfer jets*

In order to maintain notation consistent with the forward mode of operation, the speed ratio S will assume negative values for the reverse mode. In this case two important

https://doi.org/10.1017/S0022112097007398 Published online by Cambridge University Press

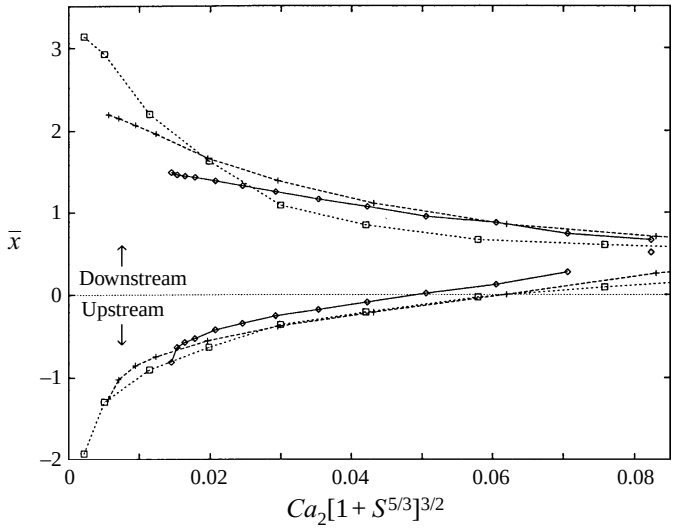


FIGURE 16. Forward-mode meniscus coating; positions of upstream and downstream menisci as functions of $(Ca_2)[1+S^{5/3}]^{3/2}$ when $\lambda_i = 0.16$ for the cases: $\diamond$, $R/H_0 = 100$, $Ca_2 = 1.45 \times 10^{-2}$; $+$, $R/H_0 = 200$, $Ca_2 = 5.60 \times 10^{-3}$; $\square$, $R/H_0 = 400$, $Ca_2 = 2.20 \times 10^{-3}$.

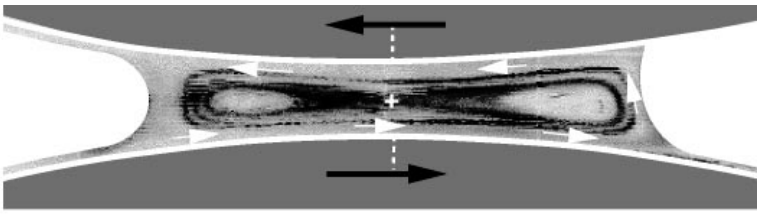


FIGURE 17. Reverse-mode meniscus coating as visualized by the laser and particle technique ($R/H_0 = 50$, $S = -1.0$, $\lambda_i = 0.12$, $Ca_2 = 2.10 \times 10^{-2}$); a primary transfer jet is seen to pass around a large eddy with two sub-eddies, a saddle at the nip and a separatrix. The broken vertical line indicates the minimum gap (nip) position.

control parameters are S and λ_i which, when varied, are observed to generate three distinct flow structures, figures 17, 18 and 19. With $S = -1$ and $\lambda_i = 0.12$, figure 17 shows a large eddy pinned to the upstream meniscus and circumnavigated by a primary fluid transfer jet conveying fluid to the the upper roll – the inlet film travels the length of the bead, splitting at the downstream meniscus. On closer inspection this large eddy is seen to consist of two sub-eddies enclosed by a separatrix with its saddle point located at the nip.

Experimentally it is found that two critical events will arise when each of the two control parameters is varied independently. If S remains fixed and λ_i is increased, the eddy is 'squeezed' by the primary transfer jet until a critical flow rate, λ_{is}, is reached. At this point there emerges a secondary transfer jet taking fluid between the two sub-eddies to the upper roll – see figure 18 with $S = -1$ and $\lambda_i = 0.3$. In practice both rolls were run at constant speed, the inlet flux also remained constant and a variable flow rate was achieved by changing the minimum gap, H_0.

A second critical event arises when speed ratio S is gradually decreased while maintaining a fixed flow rate. This is achieved by keeping the lower roll speed constant and varying the speed of the upper roll. As S decreases the downstream meniscus

https://doi.org/10.1017/S0022112097007398 Published online by Cambridge University Press

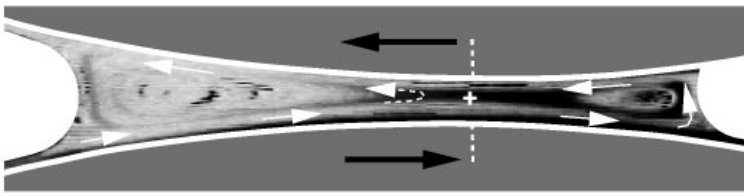


FIGURE 18. Laser illuminated dye trace of reverse-mode meniscus coating showing the co-existence of both primary and secondary transfer jets ($R/H_0 = 100$, $S = -1.0$, $\lambda_i = 0.30$, $Ca_2 = 2.20 \times 10^{-2}$); the + indicates the approximate location of the saddle point. The broken vertical line indicates the minimum gap (nip) position.

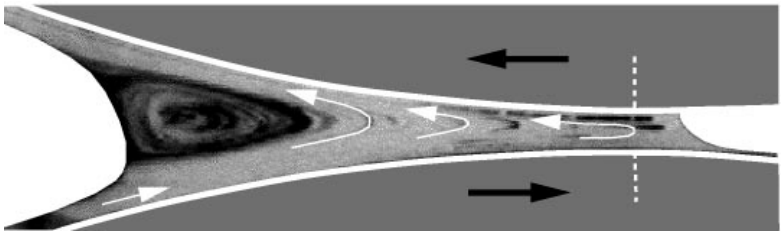


FIGURE 19. Reverse-mode meniscus coating for the case when there is no longer a downstream eddy; the downstream meniscus has advanced towards the nip and the primary and secondary transfer jets have merged ($R/H_0 = 100$, $S = -2.0$, $\lambda_2 = 0.45$, $Ca_2 = 5.50 \times 10^{-2}$). The broken vertical line indicates the minimum gap (nip) position.

approaches the nip and a critical point $\lambda_{ia}(S)$ is reached when the downstream sub-eddy becomes so small that the centre and the saddle coalesce and annihilate to leave a single eddy attached to the upstream meniscus, as illustrated in figure 19 with $S = -2$ and $\lambda_i = 0.45$. It is interesting to note that unlike the forward-mode case, the secondary transfer jet does not seem to grow at the expense of the primary one, rather the two appear to merge once the downstream sub-eddy disappears.

Figure 20 shows the two critical flow rates λ_{is} and λ_{ia} as a function of speed ratio S together with schematics representing typical flow structures in the three regions [I], [II], [III] of parameter space. Experimental data close to the critical curves are subject to the same dye injection observation threshold and pseudo-jet effects as described earlier.

Sub-eddy–saddle annihilation was observed for $R/H_0 = 100$ over a range of speed ratios, $S \in (-2.5, -1.5)$ and capillary numbers $Ca_2 \in (3.8 \times 10^{-3},\ 3.4 \times 10^{-2})$. The emergence of the secondary transfer jet was obtained for almost constant flow rate (independent of S). The two curves intersect at a point where the two critical events happen simultaneously and the speed ratio where this occurs is referred to as S_{crit}, the value of which depends on Ca_2 and R/H_0.

4.2. *Meniscus location and bead break; film thickness measurement*

The dependence on capillary number, Ca, of the location and extent of the coating bead is illustrated in figure 21. For two values of the geometry parameter, $R/H_0 =$ 100, 200, this is achieved by keeping the lower roll speed constant (hence maintaining a constant flow rate, $\lambda_i = 0.24$ and 0.5, respectively) and increasing the speed of the upper roll only. As Ca increases, the upstream meniscus moves out initially and subsequently moves in – yet fails to reach the nip – unlike the forward roll case.

https://doi.org/10.1017/S0022112097007398 Published online by Cambridge University Press

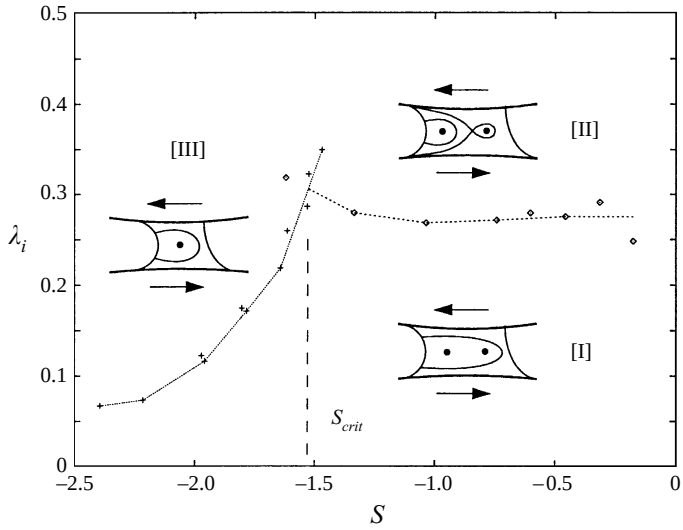


FIGURE 20. Experimentally determined λ_i, S control space diagram for reverse-mode coating: $\diamond$, points (λ_{is}) found by holding Ca_2 constant ($= 1.65 \times 10^{-2}$) and varying R/H_0; +, points (λ_{ia}) found by fixing R/H_0 ($= 100$) and varying S. Typical flow structures are shown schematically for the three regimes defined by the two curves.

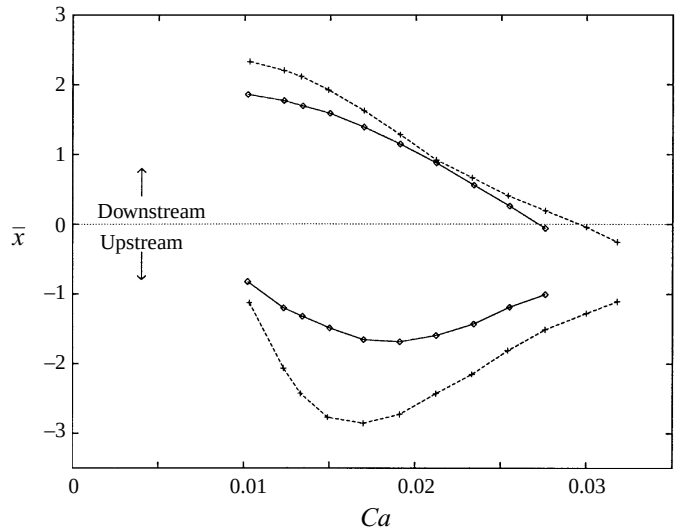


FIGURE 21. Reverse-mode meniscus coating; upstream and downstream meniscus positions as a function of Ca for $\diamond$, $R/H_0 = 100$ ($\lambda_i = 0.24$, $Ca_2 = 2.05 \times 10^{-2}$); +, 200 ($\lambda_i = 0.50$, $Ca_2 = 2.05 \times 10^{-2}$).

The downstream meniscus, on the other hand, continues to approach the nip almost linearly with Ca and, once through the nip, bead break ensues immediately.

In parallel with the above behaviour there are changes to the film thicknesses H_1 and H_2, attached to the upper and lower rolls. Figure 22 shows data for the case $R/H_0 = 100$: as $|S|$ increases from 0 to 2.0, H_2/H_0 decreases monotonically from an initial value of 0.48 to approximately 0.1 whereas H_1/H_0 initially increases – reaches

https://doi.org/10.1017/S0022112097007398 Published online by Cambridge University Press

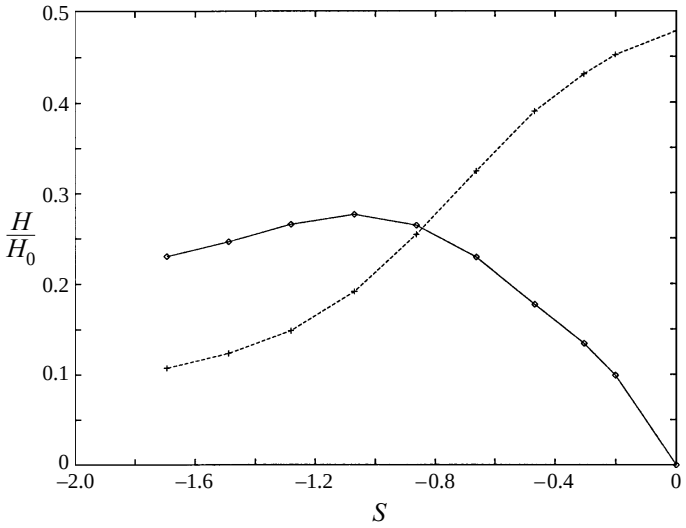


FIGURE 22. Non-dimensional film thicknesses ($\diamond$, H_1/H_0; +, H_2/H_0) as a function of S for reverse-mode coating($R/H_0 = 100$, $\lambda_i = 0.24$, $Ca_2 = 2.05 \times 10^{-2}$).

a maximum (0.28) – and then falls to approximately 0.22. This maximum value of H_1/H_0 appears to arise when the upstream meniscus is furthest from the nip.

Flow continuity and the Landau–Levich equation

A partial explanation for the above trends and features follows from two simple equations. Continuity of flow relates film thicknesses H_1 and H_2 to the inlet film H_i and speed ratio S:

$$U_2 H_i = U_1 H_1 + U_2 H_2,$$

hence

$$H_i = S H_1 + H_2. \tag{4.1}$$

Also the Landau–Levich equation (Landau & Levich 1942) provides, for small capillary numbers, a useful way of relating the thickness of a uniform film emerging from a coating bead to the radius, $\mathscr{R}$, of the associated meniscus and roll speed, U:

$$H = 1.34 \left(\frac{\mu U}{\sigma} \right)^{2/3} \mathscr{R}. \tag{4.2}$$

Hence if $\mathscr{R}_u$, $\mathscr{R}_d$ are the radii of curvature of the upstream and downstream menisci, respectively

$$H_1 = 1.34 \left(\frac{\mu U_1}{\sigma} \right)^{2/3} \mathscr{R}_u, \quad H_2 = 1.34 \left(\frac{\mu U_2}{\sigma} \right)^{2/3} \mathscr{R}_d. \tag{4.3}$$

In turn, $\mathscr{R}_u$ and $\mathscr{R}_d$ can be expressed approximately in terms of $H(X_u)$ and $H(X_d)$, the gap thicknesses at the two menisci

$$H(X_u) \approx 2\mathscr{R}_u + H_1 + H_i, \tag{4.4}$$

and

$$H(X_d) \approx \mathscr{R}_d + H_2, \tag{4.5}$$

where a 90° contact angle is assumed at the dynamic contact line. Substituting for

https://doi.org/10.1017/S0022112097007398 Published online by Cambridge University Press

$\mathscr{R}_d$ into (4.5) gives

$$H(X_d) \approx \left[1 + \frac{Ca_2^{-2/3}}{1.34}\right] H_2. \tag{4.6}$$

(i) With the upper roll at rest, $S = 0$, the inlet flux ($\lambda_i \approx 0.24$) passes straight through the nip and exits in a film of thickness $H_2/H_0 = 0.48$ on the lower roll. When the upper roll is set in motion some fluid is immediately transferred to the upper roll and so H_2 falls. Hence $H(X_d)$ decreases, via (4.6), and the downstream meniscus moves towards the nip. As S increases, more fluid is transferred, H_2 continues to fall and so the meniscus migrates towards the nip – as observed in figure 22.
The above argument rests on the validity of equation (4.6). This can easily be checked by writing it in the form

$$1 + \frac{X_d^2}{2RH_0} \approx \left[1 + \frac{Ca_2^{-2/3}}{1.34}\right] \frac{H_2}{H_0}$$

and substituting numerical values for $X_d/(2RH_0)^{1/2}$, Ca_2 and H_2/H_0 from figures 21 and 22.

(ii) At the upstream end H_1 increases when the upper roll is set in motion and the upstream meniscus is observed to move out, figure 21. However H_1 cannot increase indefinitely with S since SH_1 is bounded ($SH_1 < H_i$ via (4.1)). Hence, at some point H_1 must fall and so $\mathscr{R}_u$ decreases via equation (4.3) and also $H(X_u)$ via equation (4.4). Consequently the upstream meniscus will move in towards the nip, as observed in figure 21.

5. Pressure profiles

A key feature of forward-mode meniscus roll coating is the sub-ambient pressure field within the coating bead, Gaskell *et al.* (1995*a*). Actually measuring such small pressures experimentally within what is a very restricted region is extremely problematic – see, for example, the work of Doremus & Piau (1983) concerning streamline visualization and pressure measurement for flow between a stationary needle and a large rotating drum. However, the special case, $S = 0$ ($\lambda = 2\lambda_i$), can be readily investigated using a simple plate–roll geometry (Malone 1992), see figure 23. Proceeding in this way avoids having to take the alternative route of locating a pressure transducer within the surface of one of the rolls – a rather costly exercise fraught with its own difficulties, the most significant of which is unacceptable losses within the pressure tapping itself, P. D. Swales (1992, personal communication).

The plate–roll apparatus is of a much larger scale than the pilot rig described in §2 in order to facilitate adequate resolution of the pressure distribution across the coating bead. It consists of a thick Perspex plate mounted directly above a large rigid roll, 250 mm in diameter and 163 mm wide, which dips into a bath of oil with the properties shown in table 2. The oil is supplied to the nip region by viscous lifting where a 'fluid bead' is formed and the flow rate is controlled by varying the roll speed and minimum gap H_0. The plate is fitted with a manometer system consisting of some 20 capillary tubes spaced 2 mm apart. The pressure profile, indicated by the oil level in the capillary tubes, was recorded for various flow rates and capillary numbers.

Figure 24 shows what happens to the pressure profile as the flow rate λ_i is varied. For small λ_i the width of the bead is much smaller and fewer manometer tubes traverse its extent; the pressure is entirely sub-ambient with an almost linear gradient

https://doi.org/10.1017/S0022112097007398 Published online by Cambridge University Press

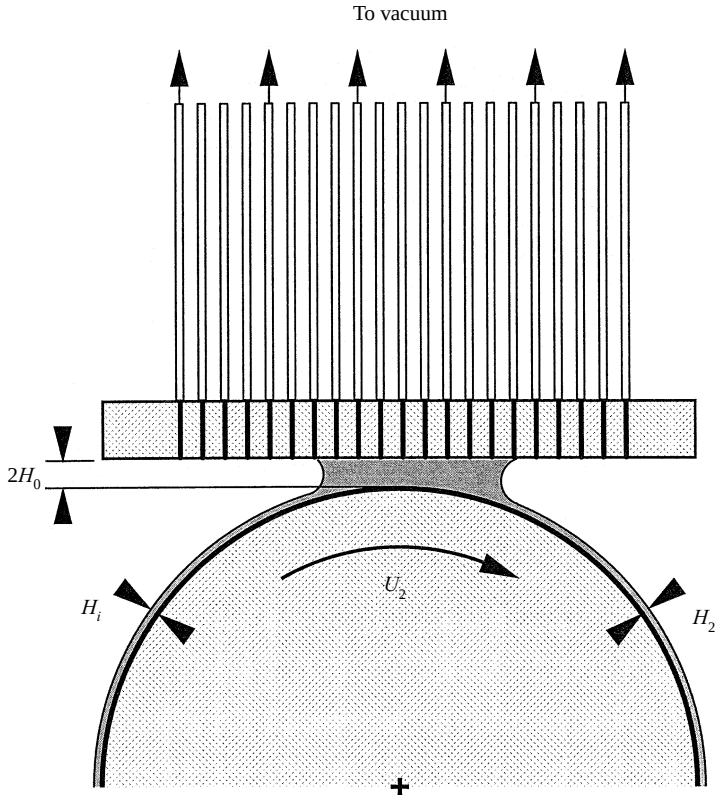


FIGURE 23. Schematic of plate–roll apparatus showing the manometer tube arrangement used to determine pressure profiles.

Surface tension	$\sigma = 4.3 \times 10^{-3}$ N m^{-1}
Density	$\rho = 839$ kg m^{-3}
Dynamic viscosity	$\mu = 7.05 \times 10^{-3}$ Pa s at $T = 20.0\,^{\circ}$C

TABLE 2. Nominal properties of the oil used in the roll–plate experiments

typical of meniscus roll coating. As λ_i increases, the upstream meniscus moves away from the nip; the magnitude of the upstream capillary pressure falls as the radius of curvature increases and hence the slope of the pressure curve falls. The transition to the inlet flooded case is observed, as λ_i continues to increase, by the emergence of pressure curves with turning points ($\lambda_i > 1$) where the pressure has both a local maximum and minimum. The maximum pressure increases with λ_i and, as the inlet approaches its fully flooded state, super-ambient pressures appear upstream of the nip and the pressure curve is typical of the classical coating regime. These results are in general agreement with the theoretical predictions of Gaskell *et al.* (1995*a*). It is interesting to note also that for this plate–roll system the location of the downstream meniscus remains relatively insensitive to changes in flux.

https://doi.org/10.1017/S0022112097007398 Published online by Cambridge University Press

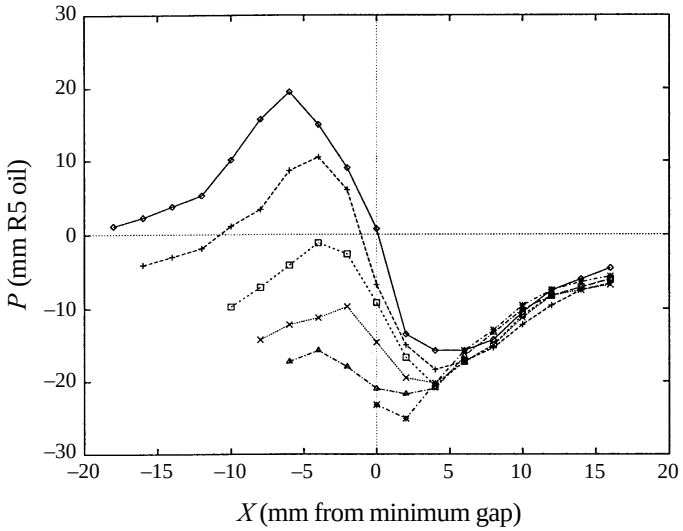


FIGURE 24. Typical pressure profiles obtained with the plate–roll apparatus for the case $S = 0$, Malone (1992), covering the range from flooded –◇– to starved - – × – - inlet conditions.

6. Effect of the feed condition

In §3.1 the effect of the feed condition on flow structure within the bead was examined for contra-rotating rolls. Once λ_i exceeds λ_{ip}, the critical flow rate for the disappearance of the primary transfer jet, figures 11 and 12 illustrate the emergence of quasi-unidirectional flow close to the nip, the extent of which increases with λ_i until the inlet becomes fully flooded and maximum flow rate is achieved.

In the case of co-rotating rolls (reverse-mode coating) the effect of the feed condition can be inferred with the aid of figure 20. Starting in region [I], where $\lambda_i < \lambda_{is}$, there is one (primary) transfer jet taking fluid to the upper roll around the perimeter of the closed eddy which is attached to the upstream free surface. Keeping S fixed, with $S > S_{crit}$, and increasing λ_i causes a secondary transfer jet to appear when $\lambda_i = \lambda_{is}$ and fluid transfer to the upper roll is by way of both a primary and secondary transfer jet (region [II]) – as for forward roll coating. If instead $S < S_{crit}$ is fixed, increasing λ_i results in the disappearance of the downstream sub-eddy ($\lambda_i > \lambda_{ia}$) once the saddle point and centre have coalesced and annihilated each other (region [III]) and so caused the primary and secondary transfer jets to merge. As the inlet flow rate, λ_i, increases the upstream meniscus moves away from the nip and eventually the inlet becomes flooded and there is 'flow back' of fluid over the top of the inlet film and back into the reservoir.

The problem with this reverse mode of operation is how to specify the extent of the meniscus coating regime. As in the forward-mode case, it will include ultra-starved inlets, $\lambda_i \leqslant \lambda_{is}$, where there is only a primary transfer jet. It will also include starved inlets, $\lambda_i > \lambda_{is}$, where fluid is transferred by both primary and secondary transfer jets but, unlike the forward mode, there is no natural cut-off, or critical, λ_i value. Perhaps it is sufficient to say that inlets should remain starved and free from flow back such that the upstream meniscus does affect both the flow and pressure fields in the coating bead. A summary of the meniscus coating regimes for both forward and reverse modes is given in table 3.

https://doi.org/10.1017/S0022112097007398 Published online by Cambridge University Press

Meniscus roll coating	Inlet condition	Fluid transfer mechanism	Flow rate
Forward mode	Ultra-starved	Primary jet	$\lambda \leqslant \lambda_{is}$
	Starved	Primary and secondary jets	$\lambda_{is} < \lambda \ll \lambda_{ip}$
Reverse mode	Ultra-starved	Primary jet	$\lambda \leqslant \lambda_{is}$
	Starved (no flow-back)	Primary and secondary jets	$\lambda_{is} < \lambda$

TABLE 3. Characteristic features of meniscus roll-coating regimes

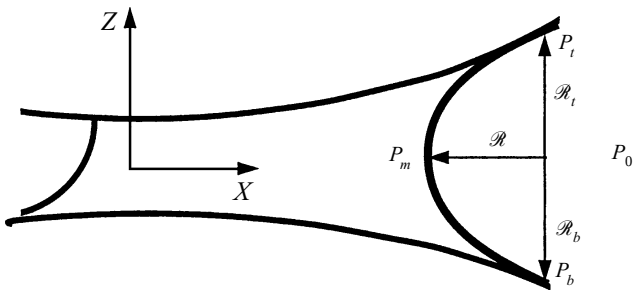


FIGURE 25. Schematic showing local radii of curvature and pressures on the downstream meniscus.

The authors are grateful to both the EPSRC and ICI for their generous support of this work. Thanks are also due to R.C. Lodge for his work in helping design the experimental apparatus, B. Malone who performed some of the early experiments and to A. Clarke of Kodak UK for advice regarding laser sectioning and particle imaging.

Appendix. Film split and gravity correction

In the flow between rolls where the gap thickness is small, $H_0/R \ll 1$, it is usually assumed that pressure and viscous stresses are dominant and the effect of gravity is negligible. An exception is in the neighbourhood of a meniscus where hydrostatic pressure will have a local effect causing a change in the local radius of curvature. In figure 25, P_0 is air pressure, while P_t, P_b and P_m represent fluid pressure on the top and bottom parts of the meniscus and at the centre ($Z = 0$) of the meniscus, respectively.

A pressure balance in each of these regions yields

$$P_m + \frac{\sigma}{\mathscr{R}} = P_0, \quad P_t + \frac{\sigma}{\mathscr{R}_t} = P_0, \quad P_b + \frac{\sigma}{\mathscr{R}_b} = P_0, \tag{A 1}$$

where $\mathscr{R}_t$, $\mathscr{R}_b$ and $\mathscr{R}$ refer to the local radii of curvature on the top, bottom and central parts of the downstream meniscus, respectively. Furthermore P_t and P_b will differ from P_m by hydrostatic pressure components, such that

$$P_t \approx P_m - \rho g \mathscr{R}, \quad P_b \approx P_m + \rho g \mathscr{R}. \tag{A 2}$$

Hence

$$\frac{1}{\mathscr{R}_t} = \frac{1}{\mathscr{R}} + \left[\frac{\rho g}{\sigma}\right] \mathscr{R}, \quad \frac{1}{\mathscr{R}_b} = \frac{1}{\mathscr{R}} - \left[\frac{\rho g}{\sigma}\right] \mathscr{R}, \tag{A 3}$$

and

$$\mathscr{R}_t = \mathscr{R}\left(1 + \left[\frac{\rho g}{\sigma}\right] \mathscr{R}^2\right)^{-1}, \quad \mathscr{R}_b = \mathscr{R}\left(1 - \left[\frac{\rho g}{\sigma}\right] \mathscr{R}^2\right)^{-1}. \tag{A 4}$$

https://doi.org/10.1017/S0022112097007398 Published online by Cambridge University Press

R/H_0	S	H_1	H_2	$\mathscr{R}_t$	$\mathscr{R}_b$	$\mathscr{R}$ eq. (A 4a)	$\mathscr{R}$ eq. (A 4b)	$\Delta\mathscr{R}$
	0.500	16.07	31.15	539.6	659.0	595.5	591.7	0.65%
100	0.742	18.18	25.55	472.2	543.6	507.7	503.4	0.85%
	1.042	18.12	19.58	374.2	415.7	390.9	396.6	-1.46%
	0.736	18.82	27.09	465.8	546.5	500.1	505.4	-1.05%
800	1.006	18.88	21.03	381.0	426.2	398.8	405.5	-1.69%
	1.748	16.41	11.94	229.0	241.9	232.6	237.9	-2.24%

TABLE 4. Comparison of independently calculated meniscus radius values, in units of micrometres. The data are for $R/H_0 = 100$, $Ca_2 = 6.57 \times 10^{-3}$, $\lambda_i = 0.077$ and for $R/H_0 = 800$, $Ca_2 = 7.09 \times 10^{-3}$, $\lambda_i = 0.64$. $\Delta\mathscr{R} = (1 - \mathscr{R}$ (equation (A 4a))/R (equation (A 4b)).

Equations (A 3) and (A 4) show that the effect of hydrostatic pressure is to reduce the radius of curvature on the top part of the meniscus and to increase it on the bottom part. When these expressions are used with the Landau–Levich (1942) equation relating film thickness to radius of curvature and capillary number

$$\frac{H}{\mathscr{R}} = 1.34Ca^{2/3}, \tag{A 5}$$

the following, gravity-adjusted, film split ratio is obtained:

$$\frac{H_1}{H_2} = \frac{\mathscr{R}_t}{\mathscr{R}_b}S^{2/3}, \approx \frac{\left(1 - \left[\frac{\rho g}{\sigma}\right]\mathscr{R}^2\right)}{\left(1 + \left[\frac{\rho g}{\sigma}\right]\mathscr{R}^2\right)}S^{2/3}, \tag{A 6}$$

$$\frac{H_1}{H_2} \approx \left(1 - 2\left[\frac{\rho g}{\sigma}\right]\mathscr{R}^2\right)S^{2/3}, \tag{A 7}$$

for $[\rho g/\sigma]\mathscr{R}^2 \ll 1$.

As expected, the effect of hydrostatic pressure is to decrease H_1 and increase H_2 such that H_1/H_2 is reduced by a factor $\left(1 - [2\rho g/\sigma]\mathscr{R}^2\right)$.

To get closer agreement with the theoretical curve in figure 15(a), which is based on the assumption that gravity effects can be neglected, $\mathscr{R}$ must be determined for each data point. Equation (A 5) is used to determine $\mathscr{R}_t$ and $\mathscr{R}_b$ using the experimentally measured film thicknesses, H_1 and H_2; hence $\mathscr{R}$ is found from equations (A 4). It can be seen from table 4, that the difference between these values, $\Delta\mathscr{R}$, is about 1 to 2% – of the same order of magnitude as the errors in H_1, H_2 and Ca_2. The effect of this gravity adjustment is seen in figure 15(b) where $(H_1/H_2)(1 - 2[\rho g/\sigma]\mathscr{R}^2)^{-1}$ is plotted against $S^{2/3}$ and there is now much closer agreement with experimental data.

The model gives sensible results even for $R/H_0 = 800$ and an inlet flux well above that associated with meniscus roll coating. This is because the Landau–Levich equation only requires that $Ca_2 \ll 1$.

REFERENCES

BABCHIN, A. J., CLISH, R. J. & WAHREN, D. 1981 Stability and disturbance of coating films. *Adv. Colloid Interface Sci.* **14**, 251–280.

BANKS, W. H. & MILLS, C. C. 1954 Some observations on the behaviour of liquids between rotating rollers. *Proc. R. Soc. Lond.* A **233**, 414–419.

BENKREIRA, H., EDWARDS, M. F. & WILKINSON, W. L. 1981*a* A semi-empirical model of the forward roll coating flow of Newtonian fluids. *Chem. Engng Sci.* **36**, 423–427.

https://doi.org/10.1017/S0022112097007398 Published online by Cambridge University Press

Benkreira, H., Edwards, M. F. & Wilkinson, W. L. 1981*b* Roll coating of purely viscous liquids. *Chem. Engng Sci.* **36**, 429–434.

Benkreira, H., Edwards, M.F. & Wilkinson, W.L. 1982 Mathematical modelling of the reverse and metering roll coating flow of Newtonian fluids. *Chem. Engng Sci.* **37**, 277–282.

Blake, T. D. Clarke, A. & Ruschak, K. A. 1994 Hydrodynamic assist of dynamic wetting. *AIChE J.* **40**, 229–242.

Bergh, H. J. van de 1974 A study of cavitation for a cylinder sliding against a plate. MSc thesis, University of Leeds.

Broughton, G., Egan, L. W. & Sturken, C. 1950 The reverse roll principle of coating. *Tappi* **33**, 314–317.

Christodoulou, K. N. & Scriven, L. E. 1989 *J. Fluid Mech.* **208**, 321–354.

Clarke, A. 1995 The application of particle tracking velocimetry and flow visualisation to curtain coating. *Chem. Engng Sci.* **50**, 2397–2407.

Clarke, A. 1996 Recirculating flows in curtain coating. In *First Eur. Coating Symp.* (ed. P. H. Gaskell, M. D. Savage & J. L. Summers), pp. 32–41. World Scientific Publishers.

Coyle, D. J. 1992 Roll coating. In *Modern Coating and Drying Technology* (ed. E. Cohen & E. Gutoff). VCH Publishers, New York.

Coyle, D. J., Macosko, C. W. & Scriven, L. E. 1986 Film-splitting flows in forward roll coating, *J. Fluid Mech.* **171**, 183–207.

Coyle, D. J., Macosko, C. W. & Scriven, L. E. 1990*a* Stability of symmetric film splitting between counter rotating cylinders. *J. Fluid Mech.* **216**, 437–458.

Coyle, D. J., Macosko, C. W. & Scriven, L. E. 1990*b* The fluid dynamics of reverse roll coating. *AIChE J.* **36**, 161–174.

Decré, M. 1994 Etude expérimental des comportements de léinterface dans léenduisage par rouleaux. PhD thesis, Ecole Normale Supérieure, Lab. Physique Statistique, Paris.

Decré, M., Gailly, E. & Buchlin, J.-M. 1995 Meniscus shape experiments in forward roll coating. *Phys. Fluids* **7**, 458–467.

Doremus, P. & Piau, J. M. 1983 Experimental-study of viscoelastic effects in a cylinder plane lubricated contact. *J. Non-Newtonian Fluid Mech.* **13**, 79–91.

Dussan V., E. B. 1979 On the spreading of liquids on solid surfaces: static and dynamic contact lines. *Ann. Rev. Fluid Mech.* **11**, 371–400.

Floberg, L. 1965 On hydrodynamic lubrication with special reference to sub-cavity pressures and numbers of streamers in cavitation regions. *Acta Polytechnica Scandinavia* ME19.

Gaskell, P. H., Richardson, C. A. & Savage, M. D. 1997 Meniscus reverse roll coating. *J. Fluid Mech.*, in preparation.

Gaskell, P. H., Savage, M. D., Summers, J. L. & Thompson, H. M. 1995*a* Modelling and analysis of meniscus roll coating. *J. Fluid Mech.* **298**, 113–137.

Gaskell, P. H., Savage, M. D., Summers, J. L. & Thompson, H. M. 1995*b* Flow topology and transformation in a fixed-gap symmetric forward roll coating system. In *Ninth Intl Conf. on Numerical Methods in Laminar and Turbulent Flow* (ed. P. Durbetaki & C. Taylor), pp. 984–995. Pineridge Press.

Gaskell, P. H., Savage, M. D. & Walker, D. J. 1998 An experimental investigation of asymmetric transfer jets, film-splitting and flow rates in roll coating. *Phys. Fluids*, in preparation.

Gatcombe, E. K. 1945 Lubrication characteristics of involute spur gears – a theoretical investigation. *Trans. ASME*, **67**, 177–188.

Gennes, P. G. de 1985 Wetting: Statics and dynamics, *Rev. Mod. Phys.* **57**, 827–863.

Giavedoni, M. D. & Saita, A. 1992 Inter-facial viscosity in viscous free surface flows: a sample case. *Ind. Engng Chem. Res.* **31**, 2222–2231.

Glass, J. E. & Prud'homme, R. K. 1997 Coating Rheology: component influence on the rheological response and performance of water borne coatings in roll applications. In *Liquid Film Coating* (ed. S. F. Kistler & P. M. Schweizer), pp. 137–182. Chapman and Hall.

Greener, J. & Middleman, S. 1975 A theory of roll coating of viscous and viscoelastic fluids. *Polymer Engng Sci.* **15**, 1–10.

Greener, J. & Middleman, S. 1979 Theoretical and experimental studies of the fluid dynamics of a two-roll coater. *Ind. Engng Chem. Fundam.* **18**, 35–41.

Greener, J. & Middleman, S. 1981 Reverse roll coating of viscous and viscoelastic liquids. *Ind. Engng Chem. Fundam.* **20**, 63–66.

https://doi.org/10.1017/S0022112097007398 Published online by Cambridge University Press

Ho, W. S. & Holland, F. A. 1978 Between-rolls metering coating technique, a theoretical and experimental study. *Tappi* **62**, 53–56.

Innes, G. E. 1993 An experimental and theoretical investigation of viscous lifting in tribology. PhD thesis, University of Leeds.

Kistler, S. F. & Scriven L. E. 1994 The teapot effect: sheet-forming flows with deflection, wetting and hysteresis. *J. Fluid Mech.* **263**, 19–62.

Landau, L. & Levich, B. 1942 Dragging of a liquid by a moving plate. *Acta Physicochimica URSS* **XVII**(1–2), 42.

Malone, B. 1992 An experimental investigation into roll coating phenomena. PhD thesis, University of Leeds.

Miller, J. C. & Myers, R. R. 1958 A photographic study of liquid flow in a roll nip. *Trans. Soc. Rheol.* **2**, 77–93.

Myers, R. R. & Hoffman, R. D. 1961 The distribution in the roll application of Newtonian liquids. *Trans. Soc. Rheol.* **5**, 317–328.

Pitts, E. & Greiller, J. 1961 The flow of thin liquid films between rollers. *J. Fluid Mech.* **11**, 33–50.

Richardson, C. A. 1996 A theoretical investigation of reverse roll coating. PhD thesis, University of Leeds.

Richardson, C. A., Gaskell, P. H. & Savage, M. D. 1996 New results in reverse roll coating. In *First Eur. Coating Symp.* (ed. P. H. Gaskell, M. D. Savage & J. L. Summers), pp. 62–72. World Scientific Publishers.

Savage, M. D. 1982 Mathematical models for coating processes. *J. Fluid Mech.* **117**, 443–455.

Savage, M. D. 1984 Mathematical models for the onset of ribbing. *AIChE J.* **30**, 999–1002.

Schneider, G. B. 1962 Analysis of forces causing flow in roll coaters. *Trans. Soc. Rheol.* **6**, 209–221.

Schunk, P. R. & Scriven, L. E. 1997 Surfactant effects in coating processes. In *Liquid Film Coating* (ed. S. F. Kistler & P. M. Schweizer), pp. 495–536. Chapman and Hall.

Schweizer, P. M. 1988 Visualisation of coating flows. *J. Fluid Mech.* **193**, 285–302.

Schweizer, P. M. 1996 Experimental methods for coating flows. In *First Euro. Coating Symp.* (ed. P. H. Gaskell, M. D. Savage & J. L. Summers), pp. 129–157. World Scientific Publishers.

Schweizer, P. M. 1997 Experimental methods. In *Liquid Film Coating* (ed. S. F. Kistler & P. M. Schweizer), pp. 209–250. Chapman and Hall.

Shikhmurzaev, Y. D. 1993 The moving contact line on a smooth solid surface. *Intl J. Multi-phase Flow* **19**, 589–610.

Wicks, P. J., Decré, M., Planquart, Ph. & Buchlin, J. -M. 1995 Flow topology associated with disjoint eddies in an asymmetric film-splitting problem. *Phys. Rev.* E **52**, R1281–R1284.

https://doi.org/10.1017/S0022112097007398 Published online by Cambridge University Press